J. Fluid Mech. (1984), *vol.* 148, *pp.* 109–135
Printed in Great Britain

Laminar entrance flow in a curved pipe

By W. Y. SOH AND S. A. BERGER
Department of Mechanical Engineering, University of California, Berkeley, California 94720

(Received 7 February 1984 and in revised form 5 June 1984)

The full elliptic Navier–Stokes equations have been solved for entrance flow into a curved pipe using the artificial compressibility technique developed by Chorin (1967). The problem is formulated for arbitrary values of the curvature ratio and the Dean number. Calculations are carried out for two curvature ratios, $a/R = \frac{1}{7}$ and $\frac{1}{20}$, and for Dean number ranging from 108.2 to 680.3, in a computational mesh extending from the inlet immediately adjacent to the reservoir to the fully developed downstream region.

Secondary flow separation near the inner wall is observed in the developing region of the curved pipe. The separation and the magnitude of the secondary flow are found to be greatly influenced by the curvature ratio. As observed in the experiments of Agrawal, Talbot & Gong (1978) we find: (i) two-step plateau-like axial-velocity profiles for high Dean number, due to the secondary flow separation, and (ii) doubly peaked axial-velocity profiles along the lines parallel to the plane of symmetry, due to the highly distorted secondary-flow vortex structure.

1. Introduction

Fluid flow in curved pipes has attracted much attention because curved pipe or tube geometries arise in bio-fluid-mechanics, especially blood flow in the aorta, as well as in engineering applications to heat exchangers, bends in piping systems, intakes in aircraft, etc.

Unlike the flow in a straight pipe, fluid motion in a curved pipe is not parallel to the curved axis of the bend, owing to the presence of a secondary motion caused by centrifugal effects. As the flow enters a curved bend, a centrifugal force of order W^2/R acts outward from the centre of curvature on the fluid particles. Pressure gradients parallel to the axis of symmetry are almost uniform along lines normal to that symmetry axis. Because of the no-slip condition at the wall, the axial velocity in the core region is much faster than that near the wall. To maintain the momentum balance between the centrifugal force and the pressure gradient, slower-moving fluid particles must move along paths whose radii of curvature are smaller than those of faster-moving particles. This leads to the onset of a secondary flow such that fluid near the wall moves toward the inner wall along upper and lower halves of the torus wall while fluid far from it flows to the outer wall. With the addition of the mainstream motion, the fluid particles follow helical trajectories. Similar arguments can be applied to explain the winding course of open channels.

As was first discovered by Williams, Hubbell & Fenkell (1902), secondary motion shifts the location of the maximum axial velocity toward the outer wall of a curved pipe. The secondary flow enhances the flow resistance, resulting in a larger pressure drop along the bend (as compared with a straight pipe) and also expediting heat- and mass-transfer processes. An increase in momentum exchange in a curved pipe causes

the critical Reynolds number to rise as high as 7800 for a curvature ratio $a/R = \frac{1}{7}$, where a is the radius of the pipe and R the radius of curvature of the bend. Experiments of White (1919), Taylor (1929) and Adler (1934) have confirmed that the flow in a curved tube is much more stable than that in a straight pipe.

The entry flow in a curved geometry has recently become of physiological concern because of its relevance to such phenomena as the mixing of injected substances in arteries and the deposition of suspended material, such as cholesterol, on their walls. There are several controversial theories to explain the occurrence of atheromatous deposits on the vascular wall. Fry (1968, 1973) suggested that atheromatous deposits may occur in areas where wall shear is maximum. An opposing theory has been put forward by Caro, Fitz-Gerald & Schroter (1971). They maintained that deposits occur at sites of low wall shear. In helping decide the issue, it is important to obtain accurate fluid-flow quantities for the entrance flow in a curved pipe.

2. Previous investigations

Since the qualitative observation of secondary motion by Thompson (1876), in his explanation of the winding course of rivers, and by Eustice (1910, 1911), who discovered spiral motion in a curved pipe from dye-injection experiments, numerous studies on fluid flow in a curved pipe have been made for both fully developed and developing flows.

Dean (1927, 1928) may be credited with the first major theoretical advance, due to his pioneering studies on this subject for fully developed flows. Dean showed that the flow in slightly curved pipes depends primarily on a single non-dimensional parameter, first introduced by him and now called the Dean number. For small values of this parameter he developed a series solution as a perturbation of the parabolic velocity profile in a straight pipe, from which he was able to obtain a clear picture of the secondary flow streamlines and to calculate the friction ratio f_c/f_s, the ratio of the resistance in a curved pipe to that in a straight one for the same flowrate. Subsequent studies have been surveyed comprehensively by Berger, Talbot & Yao (1983). We restrict ourselves to a brief review of steady, incompressible, laminar flow in a rigid curved pipe.

2.1. *Fully developed flow*

Most of the fully developed flow analyses have been carried out on the assumption that the curvature ratio δ, equal to a/R, is small. When δ is small it can be shown (Dean 1928), as mentioned above, that the flow depends only on a single non-dimensional parameter, the Dean number. Since Dean a variety of Dean numbers have been introduced (see e.g. Berger *et al.* 1983). For the purpose of the following discussion any one of these definitions will suffice. Let us then define one of these as $D = (Ga^2/\mu)\,(2a^3/\nu^2R)^{\frac{1}{2}}$, where G is the constant pressure gradient along the bend.

Intermediate Dean number

McConalogue & Srivastava (1968) obtained numerical solutions for the range $96 < D \leqslant 600$ by a pseudospectral technique in the circumferential variable ϕ, reducing the momentum equation to an ordinary differential equation in the radial direction. The lower limit on D in their work was the upper limit in Dean's work. Truesdell & Adler (1970), Akiyama & Cheng (1971), Greenspan (1973), Austin & Seader (1973), Collins & Dennis (1975) and Dennis & Ng (1982) have reported finite-difference solutions. Extension of McConalogue & Srivastava's work has been

made by Dennis & Ng for the range $96 < D \leqslant 5000$. Interestingly enough, they found non-uniqueness in their solutions, with a four-vortex as well as two-vortex type of secondary flow appearing for $D \geqslant 956$. Masliyah (1980) had already found a four-vortex mode for a cross-section of semicircular shape with the flat surface forming the outer bend.

Large Dean number

Adler (1934) observed secondary-flow boundary layers on the two halves of the torus and inferred that the two boundary layers, on the upper and lower halves, collide at the innermost point of the cross-section, separate there, and form a reentrant jet that moves outward through the core. He claimed that f_c/f_s is proportional to $\kappa^{\frac{1}{2}}$, where $\kappa = 2\delta^{\frac{1}{2}}(aW_m/\nu)$, W_m being the mean axial velocity. We note also that this definition of Dean number is the one that will be used throughout the remainder of the paper.

Since finite-difference methods have only recently become readily accessible, and in any case become inadequate as D approaches infinity, most of the works in this category, beginning with Adler, employ boundary-layer approximations. Barua (1963) constructed a secondary flow model assuming that there are two distinct flow regions – a viscous region near the wall and an inviscid core far from it – and that the secondary flow is parallel to the plane of symmetry outside the boundary layers. He used asymptotic techniques for the main flow and the Pohlhausen integral method for the cross-flow boundary layers, patching the inner and outer solutions at the outer edge of the boundary layers. Barua found cross-flow separation at about 27° from the inner bend. Itō (1969) discovered that his boundary-layer solution breaks down near the inner bend. All of the analyses mentioned show that f_c/f_s is proportional to $\kappa^{\frac{1}{2}}$. Finally, Van Dyke (1978) speculated that high-Dean-number flow is not of conventional boundary-layer type, since he found that f_c/f_s grows like $\kappa^{\frac{1}{4}}$ from his extension by computer of Dean's series solution.

2.2. *Entry flow*

Austin (1971), Patankar, Pratap & Spalding (1974) and Humphrey (1977) carried out finite-difference calculations of the flow development in a curved pipe beginning with Poiseuille flow at the inlet. Smith (1976) also investigated the transition of a parabolic flow in a straight pipe to a curved one near their junction. Our concern is restricted to the flow development following entry into the curved pipe.

Singh (1974) obtained a series solution for the entry-flow problem valid up to a downstream distance $O(a\delta^{\frac{1}{2}})$ matching asymptotic expansions for the flows in and outside the boundary layer. He found a saddle-point-like stagnation point and a node-like sink near and at the centre of the pipe. Yao & Berger (1975), by adopting Barua's flow model, obtained a solution for the flow from the entry to the fully developed region. Like Barua, they patched the solutions for the flows inside and outside the viscous region at the outer edge of the boundary layer in the radial direction, and matched with Barua's fully developed solution, employing two different lengthscales in the streamwise direction. They found separation of the cross-flow, the extent of which increases as the flow moves downstream and then decreases monotonically as the fluid travels farther downstream (i.e. as the flow approaches Barua's solution). Liu (1977) has solved the elliptic Navier–Stokes equations numerically for one particular developing flow ($\delta = 0.2$, $Re = 200$) up to a 90° bend angle, where fully developed conditions are assumed to hold. Stewartson, Cebeci & Chang (1980) carried out boundary-layer calculations for large Dean number,

and found vanishing axial shear at the inner bend at a downstream distance $l/a = 0.943\delta^{\frac{1}{2}}$, where l is the arclength along the centreline of the bend. Since both circumferential velocity and circumferential shear were not zero at this point, these calculations supported Adler's (1934) conjecture of a reentrant jet in the cross-flow. The singular behaviour near the point of vanishing axial shear has been studied further by Stewartson & Simpson (1982).

Agrawal, Talbot & Gong (1978) measured the developing flow velocities of both axial and cross-flow components using a laser-Doppler velocimeter, and found an embedded vortex in addition to secondary flow separation near the inner bend. Choi, Talbot & Cornet (1979) performed electrochemical limited-current measurements of the local wall shear. Finding a valley in the circumferential wall-shear profile and a region of non-monotonic variation of wall shear with downstream distance, they also suggested that the vortex structure in the entry region is much more complicated than that in the fully developed flow.

3. Mathematical formulation

3.1. *Governing equations*

The equations of motion of a homogeneous fluid can be written in integral form as

$$\frac{\partial}{\partial t'}\int_{V'}\rho\boldsymbol{u}'\,\mathrm{d}V' + \int_{S'}\rho\boldsymbol{u}'(\boldsymbol{u}'\cdot\boldsymbol{n})\,\mathrm{d}S' = -\int_{S'}p'\boldsymbol{n}\,\mathrm{d}S' + \int_{S'}\boldsymbol{\tau}'\cdot\boldsymbol{n}\,\mathrm{d}S' \tag{3.1}$$

and

$$\int_{S'}\rho\boldsymbol{u}'\cdot\boldsymbol{n}\,\mathrm{d}S' = 0, \tag{3.2}$$

where ρ is the density, $\boldsymbol{u}'$ the velocity vector, p' the pressure, t' the time, $\mathrm{d}V'$ an elementary volume, $\mathrm{d}S'$ an elementary surface, $\boldsymbol{n}$ the unit outward normal vector to that surface element, and $\boldsymbol{\tau}'$ the viscous stress tensor. We shall assume that the fluid is incompressible and Newtonian, so that the viscous stress tensor is given by $\boldsymbol{\tau}' = \mu(\boldsymbol{\nabla u}' + (\boldsymbol{\nabla u}')^{\mathrm{T}})$, where μ is the viscosity, and superscript T denotes transpose. By using the Gauss divergence theorem and non-dimensionalizing the quantities $\boldsymbol{u}'$, p', $\boldsymbol{r}'$ (position vector) and t' by W_0, ρW_0^2, a, and a/W_0 respectively, (3.1) and (3.2) are reduced to the Navier–Stokes equations for an incompressible, homogeneous fluid flow:

$$\frac{\partial\boldsymbol{u}}{\partial t} + (\boldsymbol{u}\cdot\boldsymbol{\nabla})\boldsymbol{u} + \boldsymbol{u}(\boldsymbol{\nabla}\cdot\boldsymbol{u}) = -\boldsymbol{\nabla}p + \frac{1}{Re}\boldsymbol{\nabla}^2\boldsymbol{u} \tag{3.3}$$

and

$$\boldsymbol{\nabla}\cdot\boldsymbol{u} = 0, \tag{3.4}$$

where W_0 is a velocity to be defined in §3.2 and Re is the Reynolds number, defined as aW_0/ν (unprimed quantities are the corresponding non-dimensional variables). The Navier–Stokes equations (3.3) and (3.4) can be rewritten in conservative form for the toroidal coordinate system (see figure 1) as follows:

radial momentum

$$\begin{aligned}\frac{\partial u}{\partial t} + \frac{1}{rB}\left[\frac{\partial}{\partial r}(rBu^2) + \frac{\partial}{\partial\phi}(Buv) + \frac{\partial}{\partial\theta}(\delta ruw) - Bv^2 - \delta r\cos\phi w^2\right] \\ = -\frac{\partial p}{\partial r} + \frac{1}{Re}\left\{\frac{1}{rB}\left[\frac{\partial}{\partial r}\left(rB\frac{\partial u}{\partial r}\right) + \frac{\partial}{\partial\phi}\left(\frac{B}{r}\frac{\partial u}{\partial\phi}\right) + \frac{\partial}{\partial\theta}\left(\frac{\delta^2 r}{B}\frac{\partial u}{\partial\theta}\right)\right]\right. \\ \left. - \frac{1}{r^2}\left(2\frac{\partial v}{\partial\phi} + u\right) + \frac{\delta\sin\phi v}{rB} + \frac{\delta^2\cos\phi}{B^2}\left(v\sin\phi - u\cos\phi - 2\frac{\partial w}{\partial\theta}\right)\right\};\end{aligned} \tag{3.5}$$

circumferential momentum

$$\frac{\partial v}{\partial t}+\frac{1}{rB}\left[\frac{\partial}{\partial r}(rBuv)+\frac{\partial}{\partial \phi}(Bv^2)+\frac{\partial}{\partial \theta}(\delta rvw)+Buv+\delta r\sin\phi w^2\right]$$
$$=-\frac{1}{r}\frac{\partial p}{\partial \phi}+\frac{1}{Re}\left\{\frac{1}{rB}\left[\frac{\partial}{\partial r}\left(rB\frac{\partial v}{\partial r}\right)+\frac{\partial}{\partial \phi}\left(\frac{B}{r}\frac{\partial v}{\partial \phi}\right)+\frac{\partial}{\partial \theta}\left(\frac{\delta^2 r}{B}\frac{\partial v}{\partial \theta}\right)\right]\right.$$
$$\left.+\frac{1}{r^2}\left(2\frac{\partial u}{\partial \phi}-v\right)-\frac{\delta\sin\phi u}{rB}-\frac{\delta^2\sin\phi}{B^2}\left(v\sin\phi-u\cos\phi-2\frac{\partial w}{\partial \theta}\right)\right\}; \tag{3.6}$$

axial momentum

$$\frac{\partial w}{\partial t}+\frac{1}{rB}\left[\frac{\partial}{\partial r}(rBuw)+\frac{\partial}{\partial \phi}(Bvw)+\frac{\partial}{\partial \theta}(\delta rw^2)+\delta rw(u\cos\phi-v\sin\phi)\right]$$
$$=-\frac{\delta}{B}\frac{\partial p}{\partial \theta}+\frac{1}{Re}\left\{\frac{1}{rB}\left[\frac{\partial}{\partial r}\left(rB\frac{\partial w}{\partial r}\right)+\frac{\partial}{\partial \phi}\left(\frac{B}{r}\frac{\partial w}{\partial \phi}\right)+\frac{\partial}{\partial \theta}\left(\frac{\delta^2 r}{B}\frac{\partial w}{\partial \theta}\right)\right]\right.$$
$$\left.+\frac{2\delta^2}{B^2}\left(\frac{\partial u}{\partial \theta}\cos\phi-\frac{\partial v}{\partial \theta}\sin\phi-\frac{w}{2}\right)\right\}; \tag{3.7}$$

continuity
$$\frac{\partial}{\partial r}(rBu)+\frac{\partial}{\partial \phi}(Bv)+\frac{\partial}{\partial \theta}(\delta rw)=0; \tag{3.8}$$

where $B=1+\delta r\cos\phi$. The non-dimensional viscous stress tensor $\boldsymbol{\tau}$, defined as $a\boldsymbol{\tau}'/\mu W_0$, is

$$\boldsymbol{\tau}=\begin{bmatrix}\tau_{rr} & \tau_{r\phi} & \tau_{r\theta}\\ \tau_{\phi r} & \tau_{\phi\phi} & \tau_{\phi\theta}\\ \tau_{\theta r} & \tau_{\theta\phi} & \tau_{\theta\theta}\end{bmatrix},$$

where

$$\left.\begin{aligned}
\tau_{rr}&=2\frac{\partial u}{\partial r},\\
\tau_{r\phi}=\tau_{\phi r}&=\frac{\partial v}{\partial r}+\frac{1}{r}\frac{\partial u}{\partial \phi}-\frac{v}{r},\\
\tau_{r\theta}=\tau_{\theta r}&=\frac{\delta}{B}\frac{\partial u}{\partial \theta}+\frac{\partial w}{\partial r}-\frac{\delta\cos\phi w}{B},\\
\tau_{\phi\phi}&=\frac{2}{r}\left(\frac{\partial v}{\partial \phi}+u\right),\\
\tau_{\phi\theta}=\tau_{\theta\phi}&=\frac{1}{r}\frac{\partial w}{\partial \phi}+\frac{\delta}{B}\frac{\partial v}{\partial \theta}+\frac{\delta\sin\phi w}{B},\\
\tau_{\theta\theta}&=\frac{2\delta}{B}\left(\frac{\partial w}{\partial \theta}+u\cos\phi-v\sin\phi\right).
\end{aligned}\right\} \tag{3.9}$$

3.2. *Boundary conditions*

Because of the ellipticity of (3.5)–(3.8), boundary conditions must be imposed for all of the boundary surfaces of the flow domain under consideration. The fluid-flow boundaries may be considered as composed of four regions, the inlet cross-section, the rigid wall surrounding the fluid, the cross-section far downstream where the flow can be assumed to be fully developed (i.e. where there is no further significant change in velocities along the bend), and the plane of symmetry.

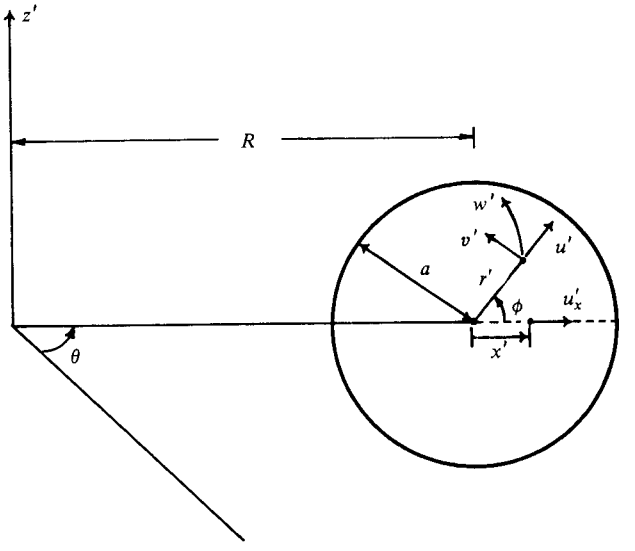

FIGURE 1. Toroidal coordinate system.

Inlet

It is impossible, strictly speaking, to give flow boundary conditions at the inlet cross-section, because the governing equations are elliptic, and therefore conditions at the inlet are influenced by conditions further downstream. To make the problem tractable we have to assume inlet flow velocities, even though this violates the ellipticity. Uniform axial velocity is one of the possible candidates for the choice of boundary conditions at the inlet section. Experiments by Agrawal *et al.* (1978) show that the flow immediately after leaving the reservoir (i.e. $\theta = 0$) develops rapidly into an inviscid vortex with its origin at the centre of curvature. An inviscid vortex profile in w will be adopted as the inlet condition in this analysis. The dimensional velocity distribution at $\theta = 0°$ is then $RW_0/(R+r\cos\phi)$. The reference velocity W_0, which has been used in non-dimensionalizing velocities in §3.1, is the axial velocity passing through $x = 0$ at the inlet, and may as well be considered as an average velocity over the cross-section for a wide range of δ, with less than 1 % error. Therefore the boundary conditions at the inlet can be written as

$$w(r,\phi,0) = \frac{1}{1+\delta r\cos\phi}, \quad u(r,\phi,0) = v(r,\phi,0) = 0. \tag{3.10}$$

Rigid wall

Owing to the no-slip condition at the wall the velocities vanish there, i.e.

$$u(1,\phi,\theta) = v(1,\phi,\theta) = w(1,\phi,\theta) = 0. \tag{3.11}$$

Far downstream

We assume that far downstream from the inlet the streamwise derivatives (i.e. $\partial/\partial\theta$) of all the velocity components vanish. In most of the calculations in the present work the axial variable $\theta_d = \pi$ is taken as 'far downstream'. Downstream axial distances θ_d are tabulated in table 1. Thus we have

$$\frac{\partial u}{\partial\theta} = \frac{\partial v}{\partial\theta} = \frac{\partial w}{\partial\theta} = 0 \quad \text{at} \quad \theta = \theta_d. \tag{3.12}$$

κ	Re	δ	θ_d	No. of steps in θ	ϵ	% error in Q
108.2	242	$\frac{1}{20}$	101°	17	0.8×10^{-4}	1.06
182.9	242	$\frac{1}{7}$	180°	25	0.8×10^{-4}	1.14
369.4	826	$\frac{1}{20}$	180°	25	0.95×10^{-4}	1.5
564.8	1263	$\frac{1}{20}$	180°	25	0.8×10^{-4}	1.7
670.8	1500	$\frac{1}{20}$	180°	25	1.0×10^{-4}	2.5
680.3	900	$\frac{1}{7}$	267°	30	1.5×10^{-4}	1.34

TABLE 1

Plane of symmetry

Owing to the existence of a plane of symmetry of the flow ($\phi = 0, \pi$), we need to solve the Navier–Stokes equations only for $0 \leqslant \phi \leqslant \pi$. The boundary conditions on the plane of symmetry are

$$\frac{\partial u}{\partial \phi} = \frac{\partial w}{\partial \phi} = 0 \quad \text{and} \quad v = 0 \quad \text{at} \quad \phi = 0, \pi. \tag{3.13}$$

4. Numerical formulation

Because of the special role of pressure, great care is needed in carrying out the numerical solution of (3.5)–(3.8). If we take the curl of the momentum equation, we get the equations of motion in terms of the vorticity and the vector potential, with the pressure eliminated. This, however, leads to great difficulties with boundary conditions, especially in three-dimensional flows. It is much easier and more accurate to use the primitive variables. Thus we employ the primitive variables u, v, w and p in this analysis.

Harlow & Welch (1965) and Williams (1969) solved the Poisson equation for the pressure by a relaxation method and a fast-Fourier-transform technique respectively. Chorin (1968) presented a pressure–velocity method which is more straightforward and efficient, and guarantees accuracy at the boundaries. Viecelli (1971), Hirt & Cook (1972), Peskin (1972) and Liu (1977) used this approach, in which flow quantities at the next time step are calculated from previous flow data by correcting the pressure successively until the continuity equation is satisfied.

4.1. *Artificial compressibility*

If the purpose is to find solely the steady-state solution of (3.5)–(3.8), it is unnecessary and computationally wasteful to solve the exact equations of motion, particularly the continuity equation, at every time step. Chorin (1967) introduced the following auxiliary system:

$$\frac{\partial \boldsymbol{u}^*}{\partial t} + [(\boldsymbol{u}^* \cdot \nabla)\boldsymbol{u}^* + \boldsymbol{u}^*(\nabla \cdot \boldsymbol{u}^*)] = -\nabla p^* + \frac{1}{Re}\nabla^2 \boldsymbol{u}^*, \tag{4.1}$$

$$\xi \frac{\partial p^*}{\partial t} + \nabla \cdot \boldsymbol{u}^* = 0. \tag{4.2}$$

With this system, $\boldsymbol{u}^*$, the solution of (4.1) and (4.2), approaches $\boldsymbol{u}$, the solution of (3.3) and (3.4), as steady state is reached. Equation (4.2) implicitly defines an artificial sound speed $V_c = W_0 \xi^{-\frac{1}{2}}$ and artificial Mach number M, where

$$M = \xi^{\frac{1}{2}} \max (u^2 + v^2 + w^2)^{\frac{1}{2}} = \xi^{\frac{1}{2}} q_{\max}.$$

It is necessary that $M < 1$, therefore

$$\xi < \frac{1}{q_{\max}^2}. \tag{4.3}$$

The numerical value of ξ, which is called the coefficient of artificial compressibility, is chosen for most rapid convergence. It plays a role similar to that of a relaxation coefficient.

Chorin's auxiliary system has enormous advantages owing to the time-explicit form of the pressure field. The merits of this method can be summarized as: (1) solution of Poisson equation for pressure, and consequently boundary conditions for pressure, are not necessary; (2) pressure–velocity iteration to satisfy continuity at every time step is not necessary; (3) inclusion of an explicit time derivative of pressure makes it possible to solve the Navier–Stokes equations by a time-marching technique, as for initial-value problems, leaving the spatial ellipticity of the equations intact (i.e. the auxiliary system of equations is parabolic in time and fully elliptic in the space dimensions); (4) simplicity in programming.

The equations to be solved are (3.5)–(3.7) together with the modified continuity equation

$$\xi \frac{\partial p^*}{\partial t} + \frac{1}{rB}\left[\frac{\partial}{\partial r}(rBu^*) + \frac{\partial}{\partial \phi}(Bv^*) + \frac{\partial}{\partial \theta}(\delta r w^*)\right] = 0 \tag{4.4}$$

(from now on we omit * for convenience) with boundary conditions (3.10)–(3.12), and initial conditions

$$u = v = 0, \quad w = \frac{1}{1+\delta r \cos\phi}, \quad p = -\frac{1}{2(1+\delta r \cos\phi)^2}. \tag{4.5}$$

Chorin (1967), Plows (1968), Fortin, Peyret & Teman (1971) and Grabowski & Berger (1976) have used this approach with various finite-difference schemes to solve fluid flow as well as heat-transfer problems.

4.2. *Finite-difference formulations*

To rewrite the momentum equations (3.5)–(3.7) and (4.4) into a practical finite-difference scheme of computation, a non-uniform staggered-grid arrangement has been chosen (see figures 2 and 3) in such a way that pressure is defined at the centre of its cell and u, v, w are defined at different positions on the pressure cell boundaries. Such a non-uniform grid was chosen because of the following considerations.

Non-uniformity in r-direction. Physically, drastic velocity changes occur near the pipe wall (i.e. $r = 1$), therefore Δr should be made small near the wall and can be made moderately large in the neighbourhood of the centre of the pipe, $r = 0$ (which is not a physical singular point, in that neither jumps nor infinite values of u, v, w and p occur there). If Δr is too small near $r = 0$, the smallest length element $r\,\Delta\phi$ becomes extremely small, of order $\Delta r\,\Delta\phi$, which jeopardizes the stability of our time-explicit computation.

Non-uniformity in ϕ- and θ-directions. Because previous work on this problem (see e.g. Berger *et al.* 1983) suggests that the flow structure is complicated near the inner bend ($\phi = 180°$), the computation in that region should be done with small $\Delta\phi$, lest the details of the inner-bend flow structure be washed out. Small values of $\Delta\theta$ near the inlet are advisable because rapid development of the main- and secondary-flow boundary layers is expected there.

Strict mass conservation in finite-difference form can be obtained by this staggered grid arrangement because no averaging is necessary on the boundaries of the pressure cell. Since the averaging process is minimized when finite-difference momentum

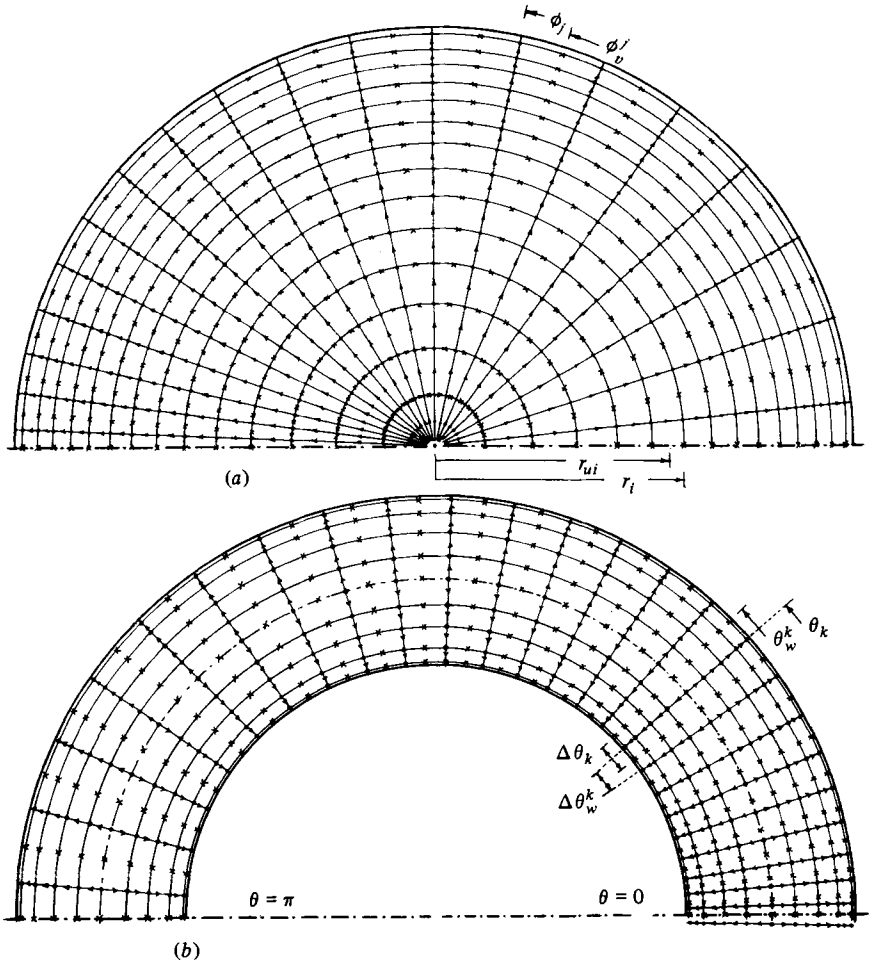

FIGURE 2. (*a*) Grid system in the cross-section: ●, p and w; ↑, u; ×, v. (*b*) Grid system on the plane of symmetry: ●, p; ↑, u; ×, w.

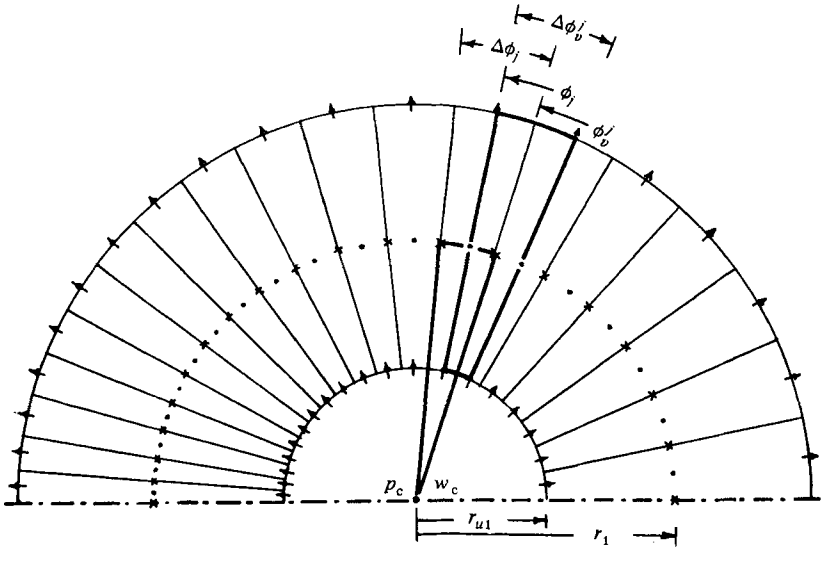

FIGURE 3. Centre cell for p and w and first ith cell for u and v: ●, p and w; ↑, u; ×, v.

equations are applied to each cell for velocity components, accuracy in the numerical computation can be enhanced.

Allen & Cheng's (1970) method for explicit differencing in time is adopted in the present analysis. Knowing u, v, w and p at $t = n\Delta t$, we can obtain these quantities at the $(n+1)$th time step. To do this, an intermediate time step $t^{\mathrm{i}} = (n+\frac{1}{2})\Delta t$ is introduced, which makes it possible to achieve second-order accuracy in t (for (3.3) and (3.4); this is an issue that is not relevant to our auxiliary system (4.1) and (4.2)) and which allows for a larger time interval Δt (Allen & Cheng 1970). Therefore an intermediate sweep is written as

$$\frac{\boldsymbol{u}^{\mathrm{i}}-\boldsymbol{u}^{n}}{\frac{1}{2}\Delta t}+\boldsymbol{F}(\boldsymbol{u}^{n}) = -\boldsymbol{G}(p^{n})+\boldsymbol{H}(\boldsymbol{u}^{n};\boldsymbol{u}^{\mathrm{i}}), \tag{4.6}$$

$$\xi\frac{p^{\mathrm{i}}-p^{n}}{\frac{1}{2}\Delta t}+D(\boldsymbol{u}^{\mathrm{i}}) = 0, \tag{4.7}$$

which is followed by a regular sweep as

$$\frac{\boldsymbol{u}^{n+1}-\boldsymbol{u}^{n}}{\Delta t}+\boldsymbol{F}(\boldsymbol{u}^{\mathrm{i}}) = -\boldsymbol{G}(p^{\mathrm{i}})+\boldsymbol{H}(\boldsymbol{u}^{\mathrm{i}};\boldsymbol{u}^{n+1}), \tag{4.8}$$

$$\xi\frac{p^{n+1}-p^{n}}{\Delta t}+D(u^{n+1}) = 0. \tag{4.9}$$

Here $\boldsymbol{F}(\boldsymbol{u})$ denotes the convection of momentum and $\boldsymbol{G}(p)$ the pressure gradient; $\boldsymbol{H}(\boldsymbol{u}^{l};\boldsymbol{u}^{m})$ is the molecular diffusion of momentum due to viscosity, evaluated at the lth time step if not at the point (i,j,k), and at the mth time step if at the point (i,j,k). $D(\boldsymbol{u})$ denotes the divergence of velocity. Decomposing (4.6)–(4.9) into components yields:

intermediate sweep

$$\frac{u^{\mathrm{i}}_{ijk}-u^{n}_{ijk}}{\frac{1}{2}\Delta t}+F_{r}(u^{n},v^{n},w^{n}) = -G_{r}(p^{n})+H_{r}(u^{n},v^{n},w^{n};u^{\mathrm{i}}_{ijk}), \tag{4.10}$$

$$\frac{v^{\mathrm{i}}_{ijk}-v^{n}_{ijk}}{\frac{1}{2}\Delta t}+F_{\phi}(u^{n},v^{n},w^{n}) = -G_{\phi}(p^{n})+H_{\phi}(u^{n},v^{n},w^{n};v^{\mathrm{i}}_{ijk}), \tag{4.11}$$

$$\frac{w^{\mathrm{i}}_{ijk}-w^{n}_{ijk}}{\frac{1}{2}\Delta t}+F_{\theta}(u^{n},v^{n},w^{n}) = -G_{\theta}(p^{n})+H_{\theta}(u^{n},v^{n},w^{n};w^{\mathrm{i}}_{ijk}), \tag{4.12}$$

$$\xi\frac{p^{\mathrm{i}}_{ijk}-p^{n}_{ijk}}{\frac{1}{2}\Delta t}+D(u^{\mathrm{i}},v^{\mathrm{i}},w^{\mathrm{i}}) = 0; \tag{4.13}$$

regular sweep

$$\frac{u^{n+1}_{ijk}-u^{n}_{ijk}}{\Delta t}+F_{r}(u^{\mathrm{i}},v^{\mathrm{i}},w^{\mathrm{i}}) = -G_{r}(p^{\mathrm{i}})+H_{r}(u^{\mathrm{i}},v^{\mathrm{i}},w^{\mathrm{i}};u^{n+1}_{ijk}), \tag{4.14}$$

$$\frac{v^{n+1}_{ijk}-v^{n}_{ijk}}{\Delta t}+F_{\phi}(u^{\mathrm{i}},v^{\mathrm{i}},w^{\mathrm{i}}) = -G_{\phi}(p^{\mathrm{i}})+H_{\phi}(u^{\mathrm{i}},v^{\mathrm{i}},w^{\mathrm{i}};v^{n+1}_{ijk}), \tag{4.15}$$

$$\frac{w^{n+1}_{ijk}-w^{n}_{ijk}}{\Delta t}+F_{\theta}(u^{\mathrm{i}},v^{\mathrm{i}},w^{\mathrm{i}}) = -G_{\theta}(p^{\mathrm{i}})+H_{\theta}(u^{\mathrm{i}},v^{\mathrm{i}},w^{\mathrm{i}};w^{n+1}_{ijk}), \tag{4.16}$$

$$\xi\frac{p^{n+1}_{ijk}-p^{n}_{ijk}}{\Delta t}+D(u^{n+1},v^{n+1},w^{n+1}) = 0. \tag{4.17}$$

4.3. *Finite differences at the centre*

A truly staggered-grid system can be obtained only by putting a nodal point at the centre (see figure 3). In the cell whose centre is at $r = 0$ special treatment for the continuity and θ-momentum equations is necessary if mass and convective momentum are to be conserved on the cell boundaries. This can be done using the integral form of the mass- and momentum-balance equations.

The non-dimensional mass-balance equation

$$\int_V \xi \frac{\partial p}{\partial t} \mathrm{d}V + \int_S (\boldsymbol{u}\cdot\boldsymbol{n})\,\mathrm{d}S = 0$$

can be written in a finite-difference form for the centre cell in figure 3 as

$$\xi \frac{\partial p_c(k)}{\partial t}\left(\frac{\pi}{2} r_{u1}^2 \frac{\Delta\theta_k}{\delta}\right) + \sum_{j=1}^{JL} u_{1j} \frac{r_{u1}\,\Delta\phi_j(1+\delta r_{u1}\cos\phi_j)\,\Delta\theta_k}{\delta} + \tfrac{1}{2}\pi r_{u1}^2 (w_c(k) - w_c(k-1)) = 0, \quad (4.18)$$

where p_c is the pressure at the centre, w_c the axial velocity at the centre, and JL the number of cells in the ϕ-direction.

From the integral momentum equation

$$\int_V \frac{\partial \boldsymbol{u}}{\partial t}\mathrm{d}V + \int_S \boldsymbol{u}(\boldsymbol{u}\cdot\boldsymbol{n})\,\mathrm{d}S = \int_V \left(-\nabla p + \frac{1}{Re}\nabla^2\boldsymbol{u}\right)\mathrm{d}V$$

we write the θ-momentum-difference equation in the form

$$\frac{\partial w_c(k)}{\partial t}\Delta V_k + \sum_{j=1}^{JL}\left(\frac{u_{1jk}+u_{1jk+1}}{2}\right)\left(\frac{w_c(k)+w_{1jk}}{2}\right)\Delta S_j + [w_c(\theta^+)^2 - w_c(\theta^-)^2]\,\Delta S_k + \delta w_c(k)\frac{u_{x0}(k)+u_{x0}(k+1)}{2}\Delta V_k = \frac{p_c(k)-p_c(k+1)}{\Delta\theta_w^k/\delta}\Delta V_k + \left[\frac{1}{Re}\int_V \nabla^2\boldsymbol{u}\,\mathrm{d}V\right]_{\theta\text{-component}}, \quad (4.19)$$

where

$$\Delta V_k = \tfrac{1}{2}\pi r_{u1}^2 \frac{\Delta\theta_w^k}{\delta}, \quad \Delta S_j = r_{u1}\Delta\phi_j \frac{(1+\delta r_{u1}\cos\phi_j)\,\Delta\theta_w^k}{\delta}, \quad \Delta S_k = \tfrac{1}{2}\pi r_{u1}^2,$$

$w_c(\theta^+)$ and $w_c(\theta^-)$ are axial velocities at the downstream and upstream faces of the centre cell, and u_{x0} is the value of u_x at the centre, u_x being defined as the velocity in the x-direction on the plane of symmetry (i.e. $u_x = u$ on $\phi = 0$, and $-u$ on $\phi = \pi$). The best numerical approximation of u_{x0} is

$$u_{x0}(k) = \tfrac{1}{2}(u_{11k} - u_{1JLk}). \quad (4.20)$$

To represent $[\int_V (\nabla^2\boldsymbol{u})\,\mathrm{d}V]_{\theta\text{-component}}$ we use a cylindrical coordinate system with origin at the centre of curvature; then

$$\left[\int_V (\nabla^2\boldsymbol{u})\,\mathrm{d}V\right]_{\theta\text{-component}} = \int_V \left\{\frac{\partial}{\partial x}\left[(1+\delta x)\frac{\partial w}{\partial x}\right] + \delta^2\frac{\partial^2 w}{\partial\theta^2} + \frac{\partial^2 w}{\partial z^2} - \delta^2 w + 2\delta^2\frac{\partial u_x}{\partial\theta}\right\}\mathrm{d}V. \quad (4.21)$$

A finite-difference form of (4.21) can be easily constructed, because the coordinate singularity that occurs at the centre for the toroidal coordinate system is removed.

Putting nodal points for p and w at the centre raises the problem of the value of

v at $r = 0$. As shown in figure 3, the v-velocity at the origin should be evaluated in order to find v and its derivatives on the ϕ^+ and ϕ^- faces in the first ith cell for the u-momentum equation, and on the r^- face in the first ith cell for the v-momentum equation. Under the assumption that $r = 0$ is not a singular point, we multiply (3.5) and (3.6) through by r^2, and, after taking the limit $r \to 0$, collect the leading terms. This yields

$$\frac{\partial^2 u}{\partial \phi^2} - 2\frac{\partial v}{\partial \phi} - u = 0, \quad \frac{\partial^2 v}{\partial \phi^2} + 2\frac{\partial u}{\partial \phi} - v = 0, \tag{4.22}$$

with boundary conditions $\partial u/\partial \phi = 0$, $v = 0$ at $\phi = 0$ and π. Exact solutions for these two equations are

$$u = A(\theta)\cos\phi, \quad v = -A(\theta)\sin\phi, \tag{4.23}$$

$A(\theta)$ is $u_{x0}(\theta)$; its best approximation $u_{x0}(k)$ is described by (4.20). Therefore the v-velocities on the ϕ^+ and ϕ^- faces become

$$\tfrac{1}{2}(v_{1j+1k} - u_{x0}(k)\sin\phi_v^{j+1}) \quad \text{and} \quad \tfrac{1}{2}(v_{1jk} - u_{x0}(k)\sin\phi_v^{j})$$

respectively, in the first ith cell for the u-momentum equation; the v-velocity on the r^- face in the first ith cell for the v-momentum equation is $\frac{1}{2}(v_{1jk} + u_{x0}(k)\sin\phi_{j-1})$.

5. Results and discussion

Calculations were carried out for Dean numbers lying in the range $108.2 \leqslant \kappa \leqslant 680.3$ for the values $\delta = \frac{1}{7}$ and $\frac{1}{20}$. A central-difference scheme was employed for the cross-flow velocities u and v. Central differencing in w was used also for the first four steps in θ (i.e. up to $\theta = 10.5°$) for the case of $\delta = \frac{1}{7}$, and for $w \leqslant 0.15$ for any δ and θ. Upwind differencing in w was used for $w \geqslant 0.15$. The computation was considered complete when the fractional changes in the radial velocities $|(u^{n+1} - u^n)/u^n|$ on the plane of symmetry were less than the values of the convergence criterion, say ϵ. The non-dimensional flow rate for each cross-section Q_k was calculated at the end of the computation as

$$Q_k = \int_0^{\pi}\int_0^1 w_k r \, \mathrm{d}r \, \mathrm{d}\phi.$$

The convergence criterion ϵ and the maximum percentage error in the flow rate, which occurs at $\theta = \theta_d$, are listed in table 1 for the different values of δ and Re.

The coefficient of artificial compressibility ξ and the time step Δt were taken as 0.3 and 0.006 respectively. Non-uniform 14×19 intervals in the r- and ϕ-directions were used throughout the calculations. The number of intervals in the θ-direction is also specified in table 1. Comparisons were made between the solutions obtained with different grid systems, and it was found that the solutions were almost the same, so that we can be reasonably confident that the present numerical calculations are independent of the grid system employed. Computations were carried out on the CDC 7600 at Lawrence Berkeley Laboratory. It usually took 9000–14 000 regular time steps for convergence, depending on the values of δ, Re and θ_d.

Axial flow development

Figures 4 and 5 show the development of the axial flow on the plane of symmetry. As the flow enters the curved bend, boundary layers begin to develop,† with the

† Of course, boundary layers may have already begun developing upstream of the inlet, but this is not accounted for in what follows.

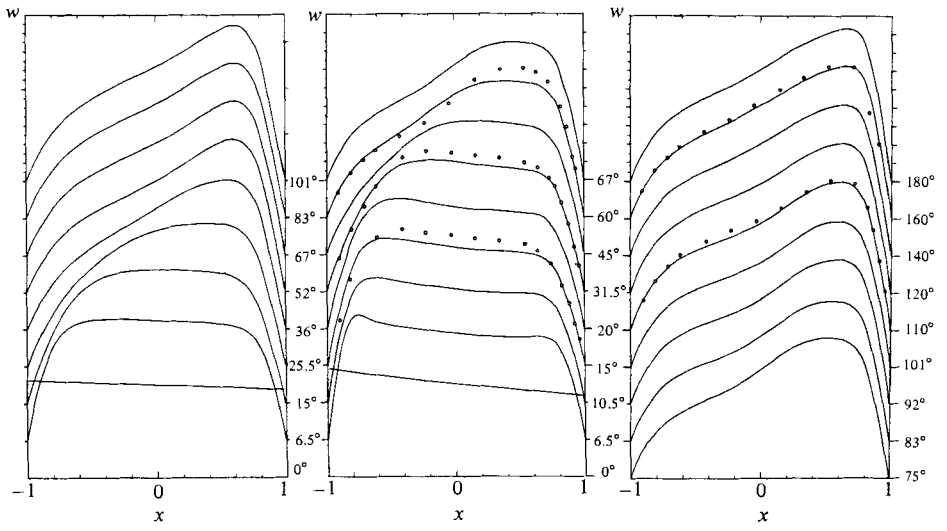

FIGURE 4. Development of axial velocity on the plane of symmetry for low κ: (*a*) $\kappa = 108.2$ ($Re = 242$, $\delta = \frac{1}{20}$); (*b*) $\kappa = 182.9$ ($Re = 242$, $\delta = \frac{1}{7}$). ——, present calculation; ○, Agrawal *et al.* (1978).

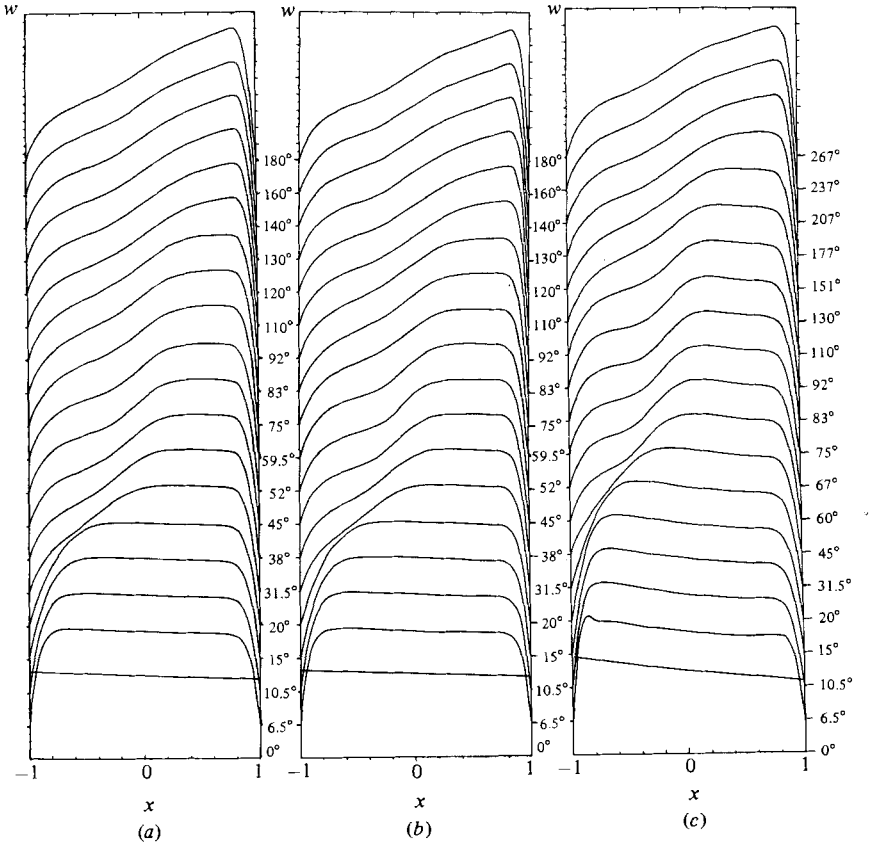

FIGURE 5. Development of axial velocity on the plane of symmetry for high κ: (*a*) $\kappa = 564.8$ (1263, $\frac{1}{20}$); (*b*) 670.8 (1500, $\frac{1}{20}$); (*c*) 680.3 (900, $\frac{1}{7}$).

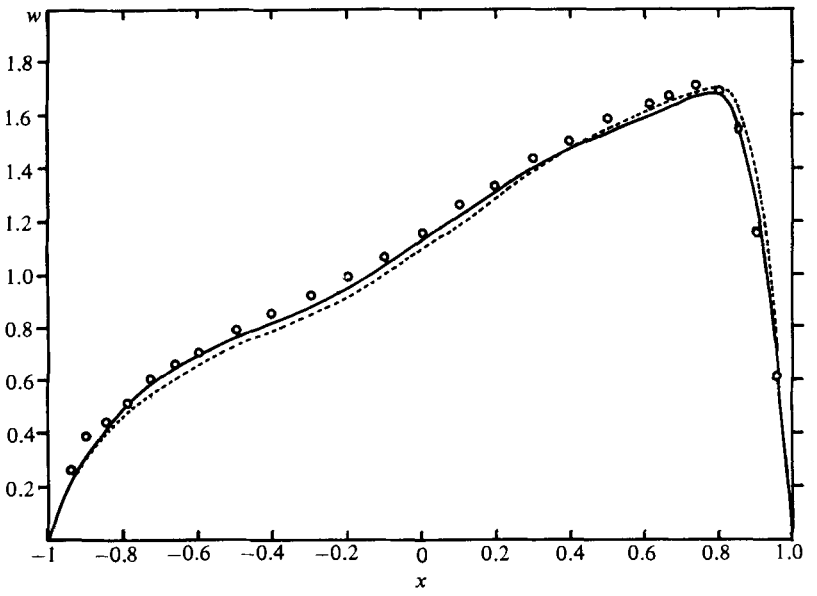

FIGURE 6. Comparison of fully developed axial velocity on the plane of symmetry: – – –, computed by Collins & Dennis (1975) for $\kappa = 369.5$; ○, measured by Adler (1934) for $\kappa = 372$; ——, present calculation for $\kappa = 369.4$ ($Re = 826$, $\delta = \frac{1}{20}$).

boundary layer near the inner bend growing much faster than that near the outer one. In the early stages of the development the potential core (the flat region in the velocity profile) appears conspicuous; this region diminishes in size as the flow develops further and far downstream the entire flow passage is occupied by the boundary layers. It is to be noted that the flat region persists much longer for the high-Reynolds-number flow than for the low-Reynolds-number flow. The location of the maximum axial velocity shifts toward the outer wall as the flow proceeds downstream.

The development of the boundary layers is greatly influenced by two factors: the molecular viscous effect and the effect of the secondary flow. Since the secondary flow transports fluid particles away from the inner wall to the outer wall through the core, the boundary layer near the inner wall of a curved pipe develops much faster than that in a straight pipe. In contrast, the development of the boundary layer near the outer wall is greatly retarded by the oncoming secondary flow, as if 'squeezed' by the flow. That is why the axial-velocity profile near the outer wall remains steep even at distances far downstream.

The smooth development of the boundary layer for moderately low κ is shown in figure 4, which illustrates how the single flat region, the inviscid core, is affected by the boundary layers. In figure 4 (*b*) comparison is made with the axial-velocity profiles measured by Agrawal *et al.* (1978). The agreement is good, improving as we move downstream. The present calculation shows very good agreement with the computation by Collins & Dennis (1975) and the experiments of Adler (1934) for $\kappa = 369.5$ (see figure 6).

As κ increases, however, two distinct flow features appear in the developing axial-velocity profile. First, in addition to a single flat inviscid core appearing right after the inlet, another flat region appears between the inner wall and the existing flat inviscid core, as if they formed two-step plateaus (see figure 5). The

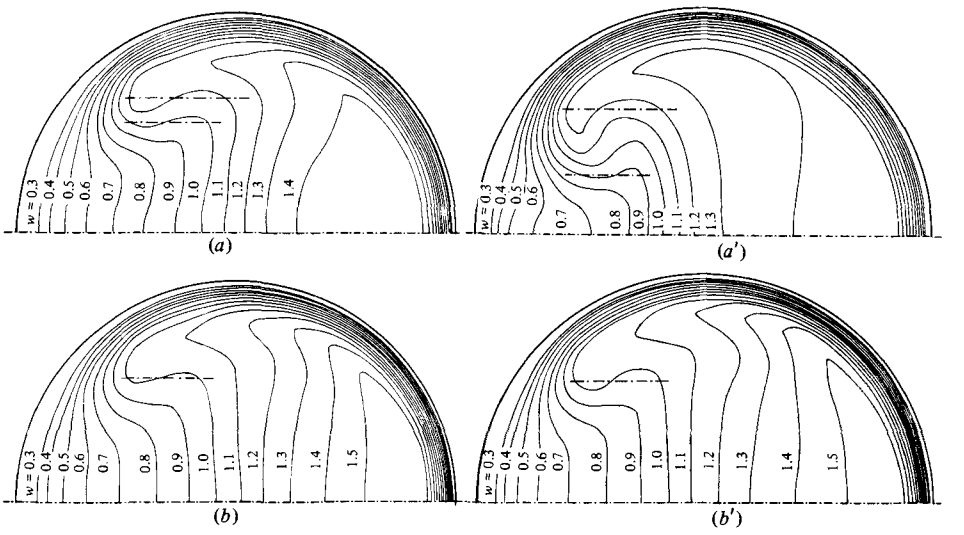

FIGURE 7. Contour of axial isovelocity for high κ: (a) at $\theta = 83°$; (b) at $\theta = 180°$ for $\kappa = 564.8$ ($Re = 1263$, $\delta = \frac{1}{20}$); (a') at $\theta = 83°$; (b') at $\theta = 267°$ for $\kappa = 680.3$ ($Re = 900$, $\delta = \frac{1}{7}$).

two-step plateaus exist for about $45°$–$60° < \theta < 110°$–$130°$ for the case $\kappa = 680.3$ ($Re = 900$, $\delta = \frac{1}{7}$), and $38° < \theta < 60°$–$75°$ for the cases $\kappa = 670.8$ ($Re = 1500$, $\delta = \frac{1}{20}$) and $\kappa = 564.8$ ($Re = 1263$, $\delta = \frac{1}{20}$).

Secondly, a double peak in the axial velocity appears on lines parallel to the plane of symmetry for high Dean numbers (see figure 7) in the developing and even fully developed regions. In the axial isovelocity contours, the isovels double back on themselves, forming the double peaks in the axial-velocity profiles. These doubly peaked velocity profiles exist for a considerable range of z, as indicated in figures 7 (a, a'), but as the flow proceeds downstream the lines on which the double peak in velocity occur shift upward away from the plane of symmetry (see figures 7b, b') such that the doubly peaked velocity profile occurs at a distance from $z = 0$. Austin & Seader (1973) reported this velocity profile for the fully developed large-κ flow. Austin (1971) observed a doubly peaked axial-velocity profile on the plane of symmetry in his studies of the flow development in a curved pipe with a parabolic entry profile. Agrawal *et al.* (1978) also found the same phenomena as the present results in their laser-Doppler experiments. For low Dean numbers the doubly peaked velocity profile does not occur (see figure 8) far downstream. These two distinct features of the axial-velocity development will be discussed later, together with a discussion of the secondary-flow development.

As for the fully developed flow, the position of the maximum axial velocity shifts more and more outward, forming a steeper velocity gradient at the outer wall; the value of the maximum axial velocity also gets smaller as the Reynolds number increases for a given δ, as shown in the last station of θ in figures 4 and 5. Patankar *et al.* (1974) also found these characteristics in their work on the flow development in a curved pipe with a parabolic entry profile. For $\delta = \frac{1}{7}$ the maximum velocities are 1.66, 1.56 and the radial positions of maximum velocity 0.67, 0.827 for $Re = 242$, 900 respectively. For $\delta = \frac{1}{20}$ the maximum velocity varies between 1.68 and 1.6 and its radial position between 0.61 and 0.843 as the Reynolds number increases from 242 to 1500.

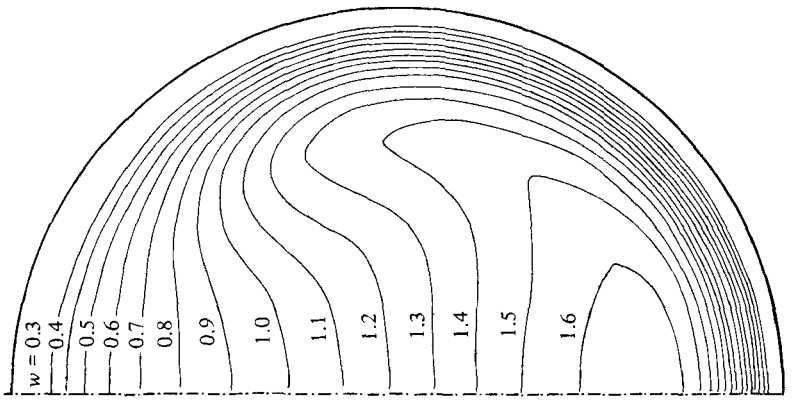

FIGURE 8. Contour of axial isovelocity for fully developed flow at $\kappa = 182.9$ ($Re = 242$, $\delta = \frac{1}{7}$).

Secondary-flow development and separation

A secondary flow is set up immediately beyond the inlet such that, as we can see in figures 9 and 10, a radial velocity of considerable magnitude occurs near the entire wall, which is analogous to the behaviour of the velocity normal to the wall near the leading edge of a flat plate. Beyond this initial zone the secondary flow near the wall begins to move circumferentially parallel to the wall, and the flow in the core region moves away from the inner wall parallel to the plane of symmetry. The magnitude of the circumferential velocity v quickly intensifies near the wall in a short distance from the inlet, and a secondary-flow boundary layer forms along the wall as if $x = 1$ were the stagnation leading edge. The circumferential-velocity profiles are shown in figure 11, in which it can be seen that as κ increases the v-velocity changes abruptly near the wall. The secondary flow develops so fast that the cross-flow attains its maximum intensity at the very early stages of flow development. For $\delta = \frac{1}{7}$, v reaches the maximum value 0.323 at $\phi = 107°$, $\theta = 55.7°$ ($l/a = 6.8$) for $\kappa = 182.9$, and 0.345 at $\phi = 135°$, $\theta = 48°$ ($l/a = 5.86$) for $\kappa = 680.3$. For $\delta = \frac{1}{20}$, v attains the maximum value 0.17 at $\phi = 84°$, $\theta = 34.75°$ ($l/a = 12.1$), and 0.193 at $\phi = 130°$, $\theta = 28.5°$ ($l/a = 9.95$) for $\kappa = 108.2$, 670.8 respectively. As the flow moves further downstream, beyond the cross-section where the maximum v occurs in the cross-flow boundary layer, the secondary flow weakens asymptotically until it becomes fully developed. At θ_d, v_{max} is 0.26 at $\phi = 96°$, 0.255 at 84°, 0.147 at 84° and 0.147 at 78° for $\kappa = 182.9$, 680.3, 108.2 and 670.8 respectively.

It is found that for a given δ the magnitude of the secondary flow is affected little by Reynolds number, at least for the Reynolds numbers considered here; that is, the intensity of the secondary flow is greatly influenced by δ and not by Re. For example, comparing the flows for $\kappa = 680.3$ and 670.8, almost-identical Dean numbers, we find that the intensity of the secondary flow for $\delta = \frac{1}{7}$ is nearly twice as large as that for $\delta = \frac{1}{20}$. For the same $\delta = \frac{1}{7}$, v_{max} for $\kappa = 182.9$ ($Re = 242$) is almost the same as v_{max} for $\kappa = 680.3$ ($Re = 900$). What the Reynolds number does affect for a given δ is the *shape* of the secondary-flow boundary layer. Although the intensity of the secondary flow rises very little as Re increases for a given δ, v changes rapidly in the boundary layer near the wall as Re increases, which means that the secondary flow near the wall takes on ever more of a boundary-layer character for large Re. Figure 11 also shows the development of the boundary layer for the cross-flow circumferentially along the wall.

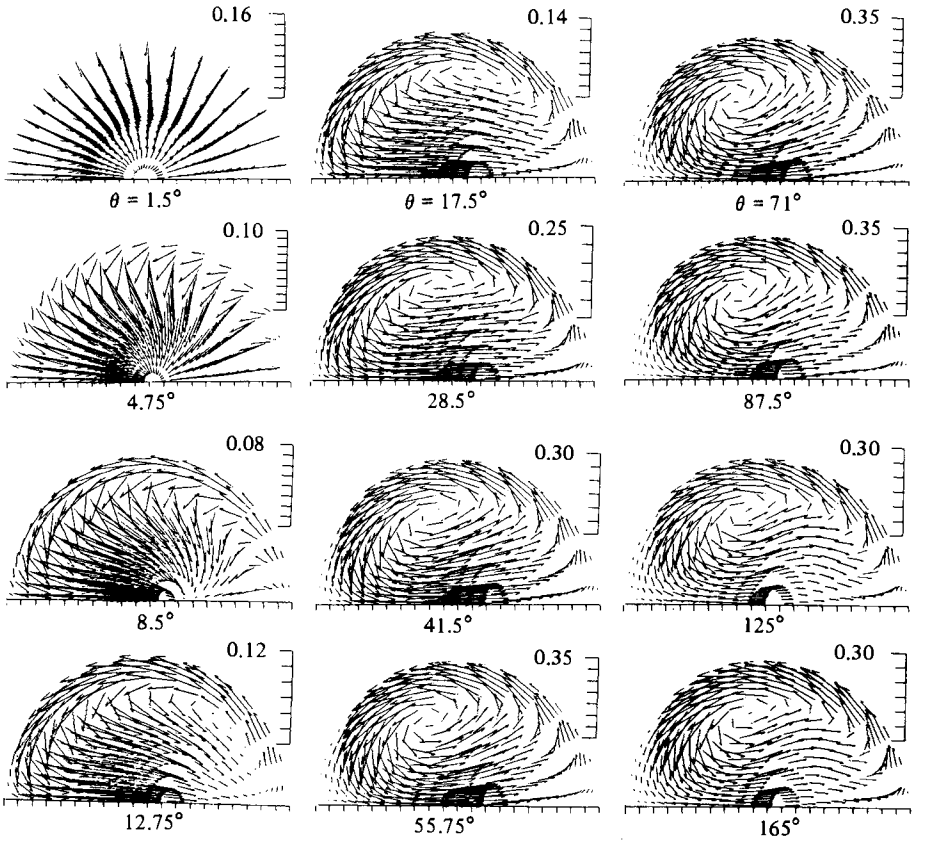

FIGURE 9. Vector plot of the secondary flow at $\kappa = 182.9$ ($Re = 242$, $\delta = \frac{1}{7}$).

Figure 12 illustrates how u_x, the cross-flow velocity at the plane of symmetry, changes with the axial coordinate θ. The present calculations show that the downstream distances where v reaches its maximum values are nearly the same as the distances at which u_x attains its maximum values.

The $\phi_{\max}$ where $v_{\max}$ occurs in the boundary layer becomes greater as κ increases. As described earlier, $\phi_{\max} = 84°$, 107°, 126°, 130° and 135° for $\kappa = 108.2$, 182.9, 564.8 ($Re = 1263$ and $\delta = \frac{1}{20}$ for this last value of κ), 670.8 and 680.3 respectively. Beyond $\phi_{\max}$ the circumferential flow along the wall should slow down to satisfy the boundary condition $v = 0$ at $\phi = 180°$. For small κ, because $\phi_{\max}$ occurs far from the inner wall, there is sufficient distance for the flow to decelerate from $v_{\max}$ to $v = 0$, so that the secondary flow can turn smoothly at the inner bend, all the while remaining attached to the circular wall. On the other hand, for large κ, the circumferential flow in the secondary-flow boundary layer does not have a sufficient distance to come to rest at $\phi = 180°$, since $\phi_{\max}$ occurs near the inner bend; furthermore, an adverse pressure gradient forms circumferentially along the wall beyond $\phi_{\max}$. Therefore separation of the secondary-flow boundary layer is inevitable near the inner wall. The plots in the second column of figure 10 show the separated recirculating regions near the inner bend. Figure 13 illustrates secondary-flow separation near the inner wall at $\theta = 79°$ for $\kappa = 680.3$. As the flow proceeds further downstream $\phi_{\max}$ shifts away from the inner bend, providing enough room for the circumferential velocity to come to rest at $\phi = 180°$, with the secondary-flow boundary layer faithfully adhering to the

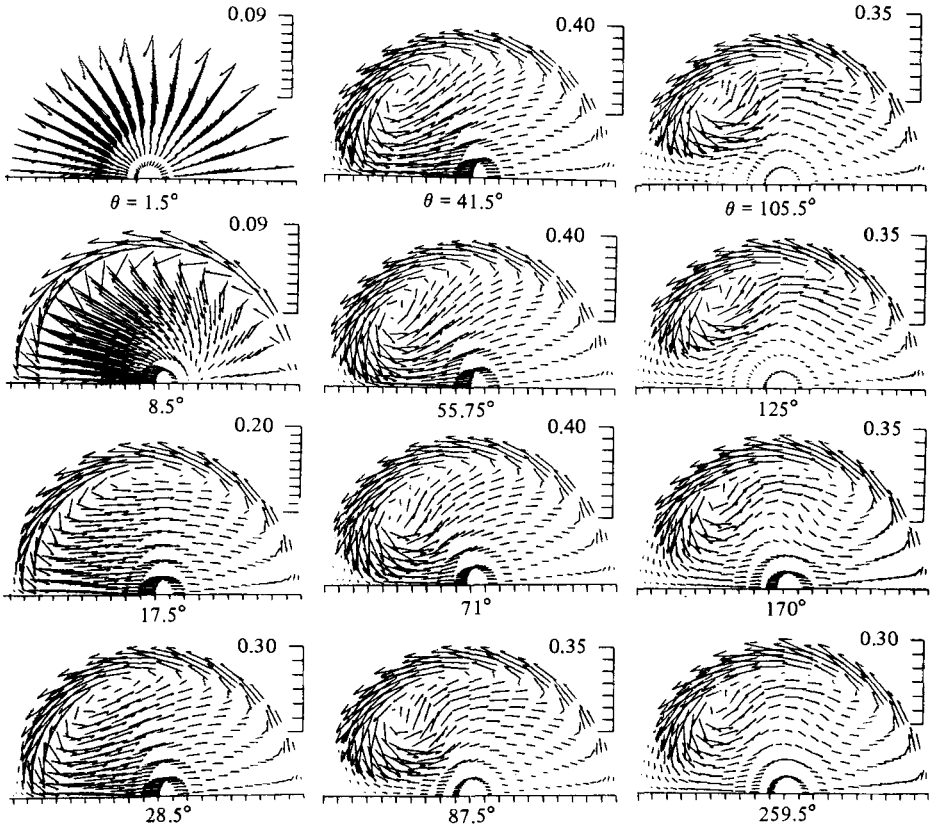

FIGURE 10. Vector plot of the secondary flow at $\kappa = 680.3$ ($Re = 900$, $\delta = \frac{1}{7}$).

wall. Thus separation of the secondary flow disappears at distances further downstream. The present study shows that this separation occurs between about $34° < \theta < 50°$, $34° < \theta < 55°$ and $45° < \theta < 96°$ for $\kappa = 564.8$, 670.8 and 680.3 respectively. It can be seen that the secondary-flow separation is much more sensitive to δ than to an increase in Re, since separation occurs over a larger axial region for $\kappa = 680.3$ ($Re = 900$, $\delta = \frac{1}{7}$) than for $\kappa = 670.8$ ($Re = 1500$, $\delta = \frac{1}{20}$). At its maximum size, the area occupied by the separation bubble is $-1 < x < -0.78$, $156.5° < \phi < 180°$ for $\kappa = 680.3$ and $-1 < x < -0.86$, $159.1° < \phi < 180°$ for $\kappa = 670.8$.

Figure 12 (*a*) illustrates the u_x profile for $\kappa = 182.9$ for different θ. We see that u_x reaches its peak at about $\theta = 48.5°$, then the u_x in the core region decreases in magnitude, forming a double peak in its profile beyond about $\theta = 96°$, and then increases again after $\theta = 130°$. Figure 12 (*b*) shows the u_x profile for the highest value of κ for which calculations have been carried out, $\kappa = 680.3$. After u_x reaches a maximum, at $\theta = 42°$, it decreases in the core region, forming multipeaks in its profile, and then far downstream oscillates in magnitude in the region away from the walls.

From these calculations we see that u_x far from the wall oscillates continuously in magnitude at distances far downstream, while the cross-flow in the secondary-flow boundary layer becomes fully developed asymptotically. Strictly speaking, the downstream boundary condition imposed at θ_d is incorrect, since u_x is not fully

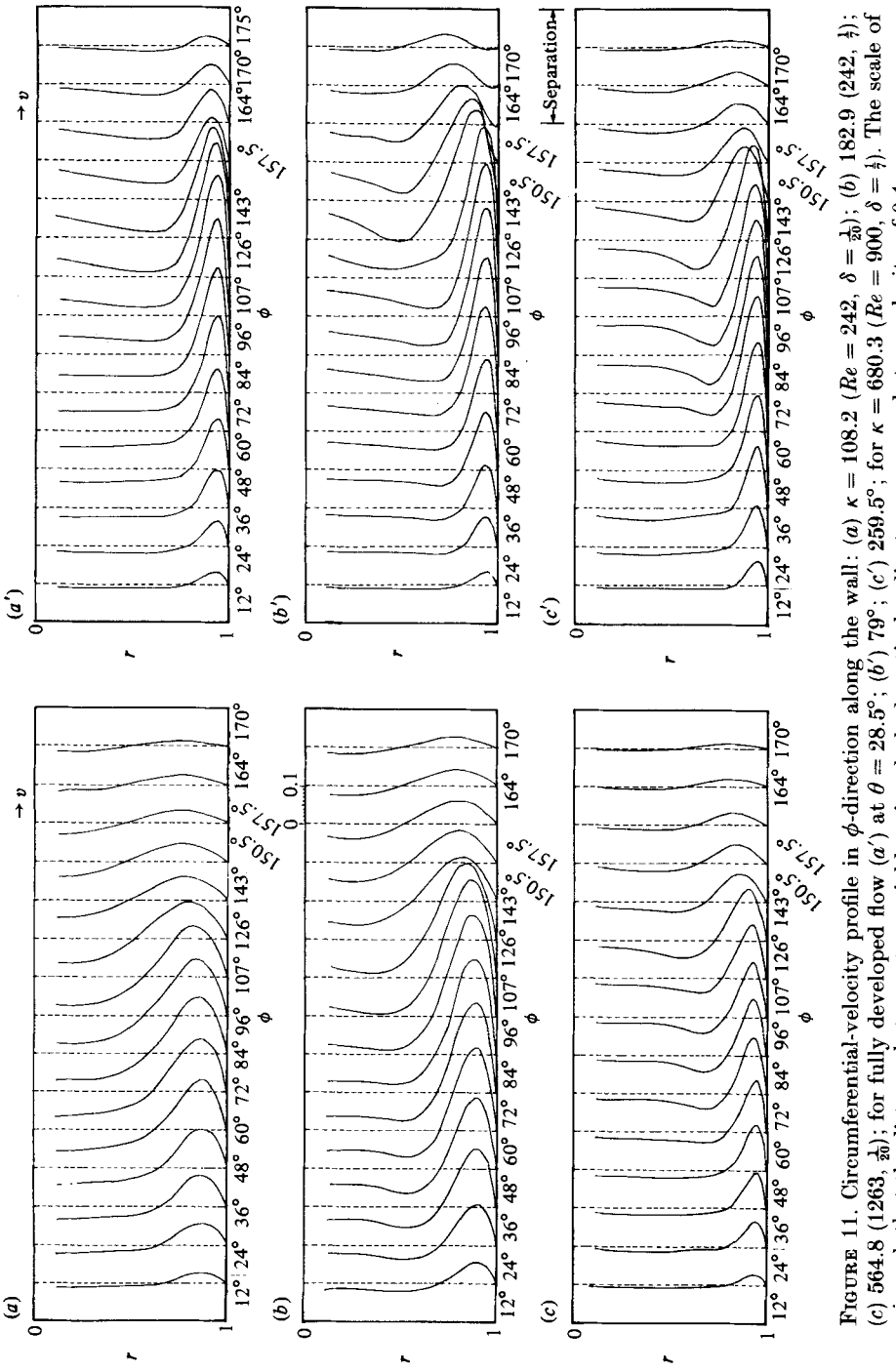

FIGURE 11. Circumferential-velocity profile in ϕ-direction along the wall: (*a*) $\kappa = 108.2$ ($Re = 242$, $\delta = \frac{1}{20}$); (*b*) 182.9 (242, $\frac{1}{7}$); (*c*) 564.8 (1263, $\frac{1}{20}$); for fully developed flow (*a'*) at $\theta = 28.5°$; (*b'*) 79°; (*c'*) 259.5°; for $\kappa = 680.3$ ($Re = 900$, $\delta = \frac{1}{7}$). The scale of v is such that the distance between two neighbouring dashed vertical ordinates corresponds to a velocity of 0.1.

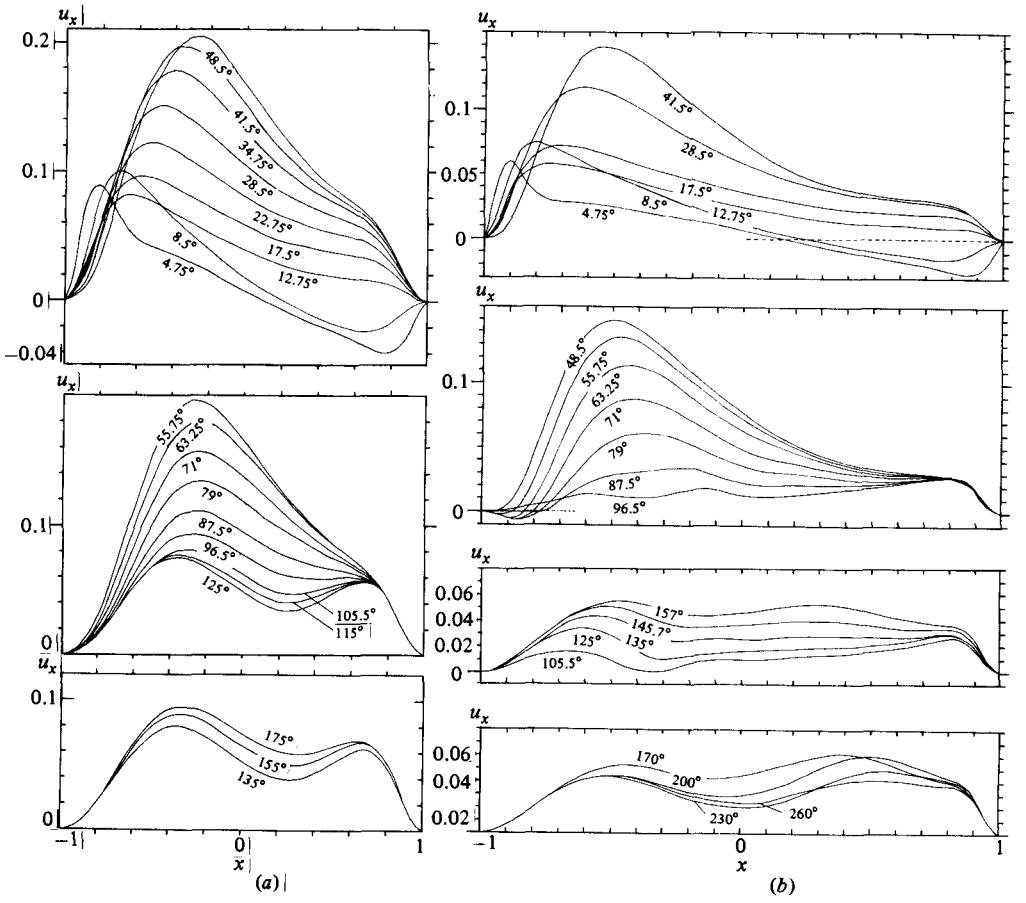

FIGURE 12. Cross-flow velocity u_x on the plane of symmetry: (*a*) $\kappa = 182.9$ ($Re = 242$, $\delta = \frac{1}{7}$), (*b*) $\kappa = 680.3$ ($Re = 900$, $\delta = \frac{1}{7}$).

developed there, owing to its oscillatory variation in the core region. In other words, a larger value of θ_d should have been assumed such that the magnitude of the oscillation in the value of u_x decreases as the flow approaches θ_d. Computationally, however, it is almost impossible to specify an arbitrarily large θ_d. Fortunately, the magnitude of the rate of change of u_x with respect to θ, although oscillating, has decayed to sufficiently small values that imposition of the downstream boundary conditions at our choice of θ_d is not bad physically. The oscillatory variation in u_x in the core region seems inviscid in character, and may eventually decay owing to viscous effects far downstream beyond our θ_d.

Secondary-flow effects on the development of the axial flow

Figure 9 shows that the secondary flow for $\kappa = 182.9$ is attached all along the wall and turns smoothly at the innermost point of the cross-section for the entire length of the pipe except the very inlet area. Therefore the axial flow develops in a smooth fashion as shown in figure 4(*b*), with no double peak in the isovelocity contour (see figure 8). For large κ, however, secondary-flow separation occurs in the developing region of θ. If separation occurs, u_x, which is negative, becomes small in that region,

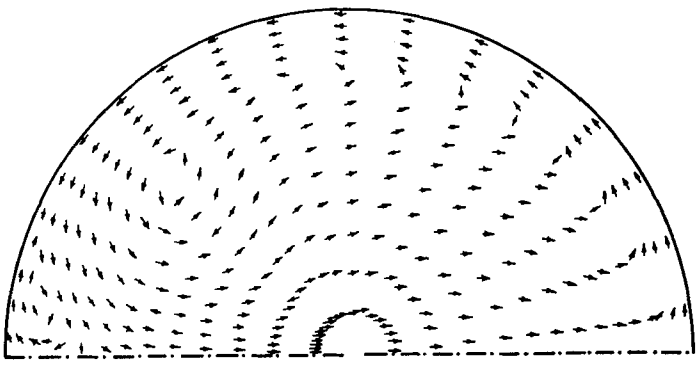

FIGURE 13. Direction plot of the secondary flow at $\theta = 79°$ for $\kappa = 680.3$.

and, near the inner wall, remains small for a considerable downstream distance θ after separation disappears (see figure 12*b*). As was mentioned earlier, two factors, the viscous effect and the cross-flow caused by the centrifugal force, assist in the axial-flow development before separation. Because, as noted above, in the separated region if this occurs, u_x is small and negative near the inner wall and remains small for some distance downstream, the secondary flow has either an adverse, in the sense of delaying the transition to the fully developed state, or negligible effect on the axial flow development near the inner wall. This adverse effect can be seen in figures 14 (*a*, *a*′), in that the axial wall shear increases a little during the separation. Therefore nearly pure viscous diffusion is the only mechanism contributing to axial-flow development. However, beyond the reattachment point on the plane of symmetry the value of u_x rises again to a considerable magnitude, and again contributes to the development of the axial flow. This may be the reason for the occurrence of the two-step plateaus in the axial flow development (see figure 5). The ratio of the slope of the plateau nearer the inner wall to the slope between the two plateaus may be considered as a rough qualitative estimate of the ratio of viscous to centrifugal effects on the axial flow development.

The secondary flow for high κ is much more distorted than that for low κ. From figures 9 and 10 we see that for any value of κ the vortex centre is shifted toward the inner wall as the flow develops, bringing it closer to the plane of symmetry. For large values of κ this effect is more conspicuous, the vortex contour near the eye being elongated, with its tail reaching close to the outer wall (see figure 10, after $\theta = 41.5°$). Beyond the separation region the vortex eye moves upward from the plane of symmetry, elongating in shape much more. In the developing region, owing to the low position of the vortex eye and its elongated tail, double peaks in the isovelocity contours appear not far from the plane of symmetry, as shown in figures 7 (*a*, *a*′). Physically what is happening is that the secondary-flow vortex conveys faster-moving fluid particles near the wall, $x > 0$, directly into the region of the vortex eye at some distance from the wall, $x < 0$. As the flow proceeds further downstream, the vortex centre moves up from the plane of symmetry, and double peaks appear only far from the plane of symmetry (see figures 7*b*, *b*′). For low κ, double-peaked velocity profiles do not appear, as can be seen from figure 8.

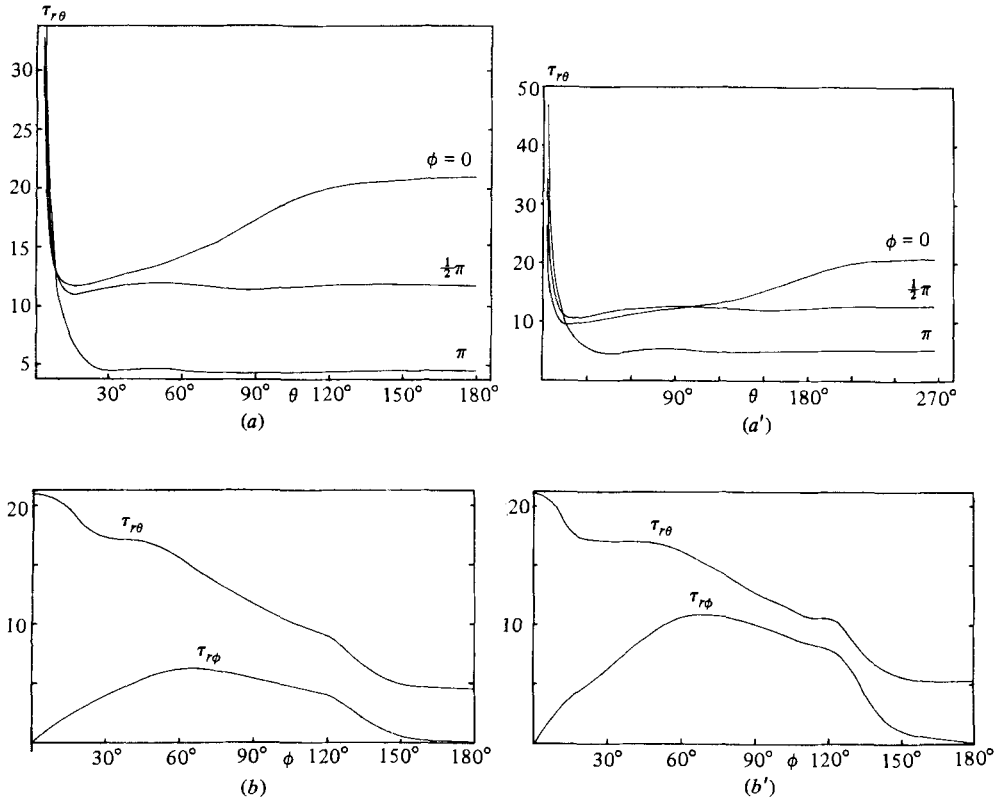

FIGURE 14. Wall shears: (*a*), (*b*) for $\kappa = 670.8$ ($Re = 1500$, $\delta = \frac{1}{20}$); (*a'*), (*b'*) for $\kappa = 680.3$ ($Re = 900$, $\delta = \frac{1}{7}$). (*b*) and (*b'*) curves are for the flow far downstream, in the fully developed region.

Pressure and wall shears

Figure 15 shows the variation of pressure along the bend for $\kappa = 680.3$. The friction ratio for the fully developed flow is calculated as

$$\frac{f_c}{f_s} = \frac{(\partial p/\partial\theta)_c}{(\partial p/\partial\theta)_s} = \frac{Re\,\delta}{8}(\partial p/\partial\theta)_c,$$

where the pressure gradient $\partial p/\partial\theta$ is calculated at θ_d. Figure 16 shows the variation of f_c/f_s with κ. It is found that the pressure gradient (or friction) in a curved pipe is 3.62 times greater than that in a straight pipe for the greatest κ in this work, $\kappa = 680.3$. Dennis (1980) corroborated Collins & Dennis's (1975) results with a new finite-difference method, and confirmed the discrepancy between their results and Van Dyke's (1978) prediction that f_c/f_s grows like $\kappa^{\frac{1}{4}}$. The present calculations agree with Collins & Dennis's results and Hasson's (1955) correlation of experiments for the range of moderately low κ, say $\kappa \leqslant 369.5$, but considerable discrepancy occurs as κ increases. This discrepancy for high κ may be explained as being caused partly by the effect of δ, and partly by the fact that in our calculations $\partial p/\partial\theta$, while almost constant, is still varying with θ even at θ_d. In other words, to obtain a truly constant pressure gradient in the present developing-flow calculations, especially for large κ, θ_d should have been chosen much larger than the value used, which is computationally extremely difficult.

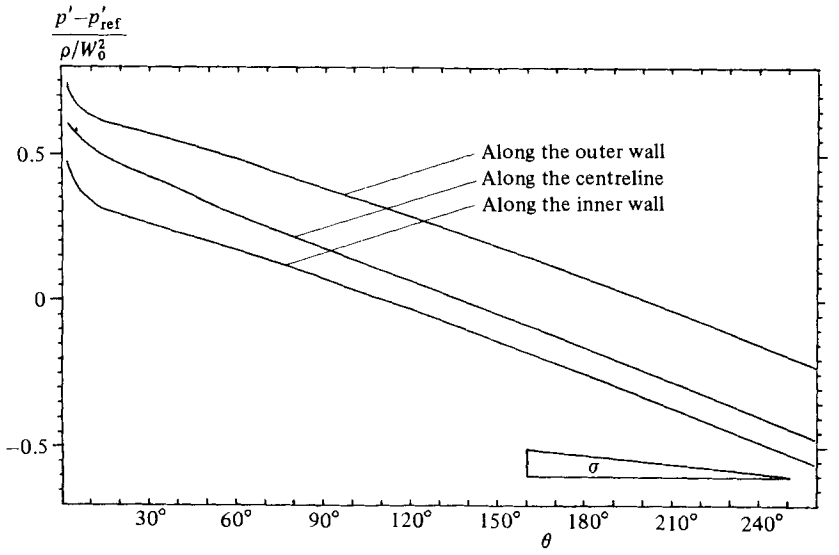

FIGURE 15. Pressure variation along the bend at $\kappa = 680.3$. $\tan\sigma = \partial p/\partial\theta$ for straight pipe.

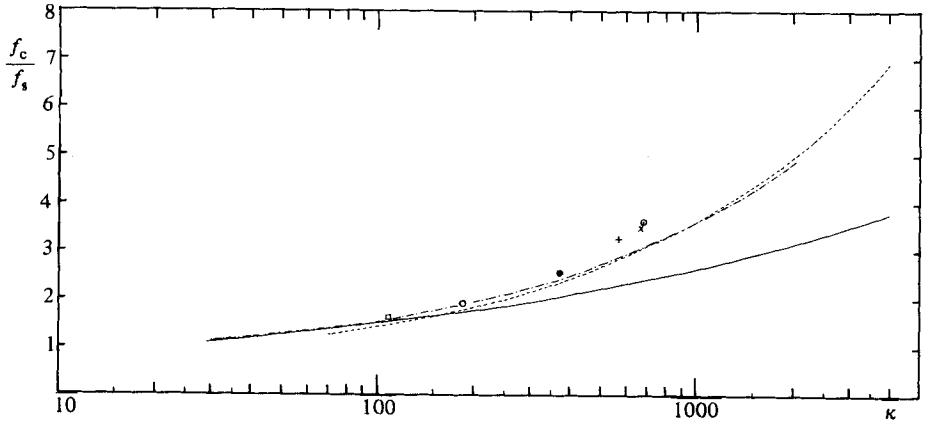

FIGURE 16. Friction ratio: ——, Van Dyke (1978); – – –, Collins & Dennis (1975); –·–·–, Hasson (1955). Present calculations: □, $\kappa = 108.2$; ○, 182.9; ●, 369.5; +, 564.8; ×, 670.8; ⊙, 680.3.

The shear stresses $\tau_{r\phi}$ and $\tau_{r\theta}$ are calculated from (3.9); at the wall these become

$$\tau_{r\phi} = \frac{\partial v}{\partial r}, \quad \tau_{r\theta} = \frac{\partial w}{\partial r}.$$

Axial wall shears $\tau_{r\theta}$ along the bend are shown in figures 14(a,a'). Initially, because of the particular entry profile used, the axial wall shear is greater at the inner wall than at the outer. The axial-wall-shear curves cross over at a very early stage of flow development along the bend, the greater shear then occurring at the outer wall. For small δ (figure 14a), crossover takes place quickly, while a longer axial distance is required for large δ. For the flows at $\kappa = 108.2$ and 670.8, in which δ is $\frac{1}{20}$, crossover occurs at $\theta = 8°$ ($l/a = 2.79$) and 8.4° ($l/a = 2.93$) respectively.

In figure 17(a) the axial variation, from this calculation, of $(\partial w/\partial\eta)_{\eta=0}$ at the

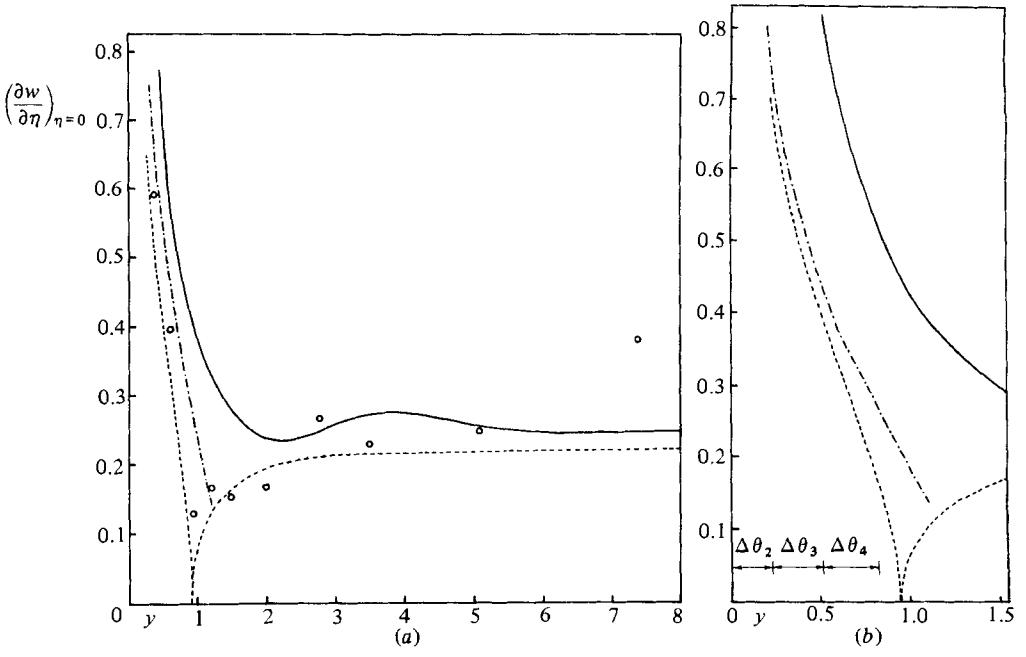

FIGURE 17. Variation of axial shear with axial distance along the pipe: ——·——, Singh (1974); – – – –, Stewartson *et al.* (1980); ——, present calculation; ○, Talbot & Wong (1982). (*a*) $\delta = \frac{1}{7}$, $Re = 900$; (*b*) $\delta = \frac{1}{20}$, $Re = 1500$.

innermost part of the bend, where η is $(1-r)(\frac{1}{2}\kappa)^{\frac{1}{2}}$, is compared with the values from the solutions of Singh (1974) and Stewartson *et al.* (1980). Also shown are the experimental data points of Talbot & Wong (1982), obtained using an electrochemical measurement technique, but for a slightly lower Dean number, $\kappa = 643$ rather than 680.3. We note, as indicated earlier, that Stewartson *et al.* found that the axial shear vanishes at some downstream location. We see from the figure that whereas Singh's and this analysis also show a precipitous drop in shear stress, neither one shows vanishing of the shear stress at any point. The experimental data follow the theoretical predictions well, exhibiting the same steep drop in axial shear, as well (see Talbot & Wong) as a general trend of decreasing axial shear with increasing κ, although, even for the highest value of κ ($\kappa = 1355$), the shear never vanishes. It should of course be borne in mind that the analysis of Stewartson *et al.* that predicts this vanishing of the shear is an asymptotic analysis valid in the limit $\kappa \to \infty$. (The Singh curve is shown only for those points where the solution is valid. It should also be noted that according to Stewartson & Simpson (1982) the part of the curve of Stewartson *et al.* beyond the point of zero axial shear is invalid.) Because the Singh and Stewartson *et al.* analyses both use the boundary-layer equations in the region immediately downstream of the entrance, it is not clear why there is a discrepancy between these two solutions near $y = 0$, where $y = (l/a)\,\delta^{\frac{1}{2}}$, unless the interaction of the boundary layer with the inviscid core is already important, an effect ignored by Stewartson *et al.*, but included in Singh. The present solution differs from both of these, but by an amount which can be accounted for by a shift of the curve by one cell in the case of Singh and two in the case of Stewartson *et al.* A shift of this amount

may reflect either the inherent indeterminacy in the calculation of the dependent variables near the first cell in a finite-difference calculation, or the fact that the boundary-layer equations are only asymptotically valid (asymptotic in distance from the leading edge). Note also that for this case $\delta = \frac{1}{7}$ and that the solutions of both Singh and Stewartson *et al.* are asymptotically valid only for small δ. Finally, we note that downstream of the point of minimum axial shear the present analysis exhibits qualitatively the same non-monotonic behaviour as the experimental data, a behaviour Talbot & Wong ascribe to the vortex structure embedded within the Dean-type secondary motion described in Choi *et al.* (1979). Figure 17 (*b*) shows the same curves for $\delta = \frac{1}{20}$. Here the Singh and Stewartson *et al.* curves lie very close to one another, possibly because for this smaller value of δ the interaction between the inviscid core and the boundary layer is minimal. The same comments apply here, as above, as to the possible explanation for the discrepancy between this work and that of Singh and Stewartson *et al.*

Circumferential wall shears $\tau_{r\phi}$ are shown in figures 14 (b, b'). For large δ, say $\delta = \frac{1}{7}$, the circumferential shear reaches values as high as 81 % of those of axial shear for $\kappa = 680.3$, and 68 % even for low Dean number, $\kappa = 182.9$. The ratio $\tau_{r\phi}/\tau_{r\theta}$ at the wall becomes smaller as δ gets smaller, its maximum value being 0.47 for $\kappa = 670.8$ and 0.35 for $\kappa = 108.2$.

The authors would like to thank Professor L. Talbot for many helpful discussions about curved-pipe flow, and Professor A. J. Chorin for his invaluable assistance in applying his artificial-compressibility method to the present problem. We also wish to acknowledge support for this research by the National Science Foundation under Grant MEA-8116360.

REFERENCES

Adler, V. M. 1934 Strömung in gekrümmten Rohren. *Z. angew. Math. Mech.* **14**, 257.

Agrawal, Y., Talbot, L. & Gong, K. 1978 Laser anemometer study of flow development in curved circular pipes. *J. Fluid Mech.* **85**, 497.

Akiyama, M. & Cheng, K. C. 1971 Boundary vorticity method for laminar forced convection heat transfer in curved pipes. *Intl J. Heat Mass Transfer* **14**, 1659.

Allen, J. S. & Cheng, S. I. 1970 Numerical solutions of the compressible Navier–Stokes equations for the laminar near wake. *Phys. Fluids* **13**, 37.

Austin, L. 1971 The development of viscous flow within helical coils. Ph.D. thesis, University of Utah, Salt Lake City.

Austin, L. R. & Seader, J. D. 1973 Fully developed viscous flow in coiled circular pipes. *AIChE J.* **19**, 85.

Barua, S. N. 1963 On secondary flow in stationary curved pipes. *Q. J. Mech. Appl. Maths* **16**, 61.

Berger, S. A., Talbot, L. & Yao, L.-S. 1983 Flow in curved pipes. *Ann. Rev. Fluid Mech.* **15**, 461.

Caro, C. G., Fitz-Gerald, J. M. & Schroter, R. C. 1971 Atheroma and arterial wall shear: observation, correlation and proposal of a shear dependent mass transfer mechanism for atherogenesis. *Proc. R. Soc. Lond.* B **177**, 109.

Choi, U. S., Talbot, L. & Cornet, I. 1979 Experimental study of wall shear rates in the entry region of a curved tube. *J. Fluid Mech.* **93**, 465.

Chorin, A. J. 1967 A numerical method for solving incompressible viscous flow problems. *J. Comp. Phys.* **2**, 12.

Chorin, A. J. 1968 Numerical solution of the Navier–Stokes equations. *Math. Comp.* **22**, 745.

COLLINS, W. M. & DENNIS, S. C. R. 1975 The steady motion of a viscous fluid in a curved tube. *Q. J. Mech. Appl. Maths* **28**, 133.

DEAN, W. R. 1927 Note on the motion of fluid in a curved pipe. *Phil. Mag.* **20**, 208.

DEAN, W. R. 1928 The streamline motion of fluid in a curved pipe. *Phil. Mag.* **30**, 673.

DENNIS, S. C. R. 1980 Calculation of the steady flow through a curved tube using a new finite-difference method. *J. Fluid Mech.* **99**, 449.

DENNIS, S. C. R. & NG, M. 1982 Dual solutions for steady laminar flow through a curved tube. *Q. J. Mech. Appl. Maths* **35**, 305.

EUSTICE, J. 1910 Flow of water in curved pipes. *Proc. R. Soc. Lond.* A **84**, 107.

EUSTICE, J. 1911 Experiments of streamline motion in curved pipes. *Proc. R. Soc. Lond.* A **85**, 119.

FORTIN, M., PEYRET, R. & TEMAN, R. 1971 Résolution numérique des équations de Navier–Stokes pour un fluide incompressible. *J. Méc.* **10**, 357.

FRY, D. L. 1968 Acute vascular endothelial changes associated with increased blood velocity gradients. *Circ. Res.* **22**, 165.

FRY, D. L. 1973 Atherogenesis: initiating factors. *Ciba Symp.* **12**, 93.

GRABOWSKI, W. J. & BERGER, S. A. 1976 Solutions of the Navier–Stokes equations for vortex breakdown. *J. Fluid Mech.* **75**, 525.

GREENSPAN, D. 1973 Secondary flow in a curved tube. *J. Fluid Mech.* **57**, 167.

HARLOW, F. H. & WELCH, J. E. 1965 Numerical calculation of time dependent viscous incompressible flow of fluid with free surface. *Phys. Fluids* **8**, 2182.

HASSON, D. 1955 Streamline flow resistance in coils. *Res. Corresp.* **1**: S1.

HIRT, C. W. & COOK, J. L. 1972 Calculating three-dimensional flow around structures and over rough terrain. *J. Comp. Phys.* **10**, 324.

HUMPHREY, J. A. C. 1977 Flow in ducts with curvature and roughness. Ph.D. thesis, Imperial College of Science and Technology.

ITŌ, H. 1969 Laminar flow in a curved pipe. *Z. angew. Math. Mech.* **49**, 653.

LIU, N.-S. 1977 Developing flow in a curved pipe. *INSERM–Euromech 92* **71**, 53.

MASLIYAH, J. H. 1980 On laminar flow in curved semicircular ducts. *J. Fluid Mech.* **99**, 469.

MCCONALOGUE, D. J. & SRIVASTAVA, R. S. 1968 Motion of fluid in a curved tube. *Proc. R. Soc. Lond.* A **307**, 37.

PATANKAR, S. V., PRATAP, V. S. & SPALDING, D. B. 1974 Prediction of laminar flow and heat transfer in helically coiled pipes. *J. Fluid Mech.* **62**, 539.

PEDLEY, T. J. 1980 *The Fluid Mechanics of Large Blood Vessels*, chap. 4. Cambridge University Press.

PESKIN, C. S. 1972 Flow patterns around heart valves: a numerical method. *J. Comp. Physics* **10**, 252.

PLOWS, W. H. 1968 Some numerical results for two-dimensional steady laminar Bénard convection. *Phys. Fluids* **11**, 1593.

SINGH, M. P. 1974 Entry flow in a curved pipe. *J. Fluid Mech.* **65**, 517.

SMITH, F. T. 1976 Fluid flow into a curved pipe. *Proc. R. Soc. Lond.* A **351**, 71.

SOH, W. Y. 1983 Laminar entrance flow in a curved pipe. Ph.D. thesis, University of California, Berkeley.

STEWARTSON, K., CEBECI, T. & CHANG, K. C. 1980 A boundary-layer collision in a curved duct. *Q. J. Mech. Appl. Maths* **33**, 59.

STEWARTSON, K. & SIMPSON, C. J. 1982 On a singularity initiating a boundary-layer collision. *Q. J. Mech. Appl. Maths* **35**, 1.

TALBOT, L. & WONG, S. J. 1982 A note on boundary-layer collision in a curved pipe. *J. Fluid Mech.* **122**, 505.

TAYLOR, G. I. 1929 The criterion for turbulence in curved pipes. *Proc. R. Soc. Lond.* A **124**, 243.

THOMPSON, J. 1876 On the origin of winding of rivers in alluvial plains, with remarks on the flow of water round bends in pipes. *Proc. R. Soc. Lond.* A **25**, 5.

TRUESDELL, L. C. & ADLER, R. J. 1970 Numerical treatment of fully developed laminar flow in helically coiled tubes. *AIChE J.* **16**, 1010.

VAN DYKE, M. 1978 Extended Stokes series: laminar flow through a loosely coiled pipe. *J. Fluid Mech.* **86**, 129.

VIECELLI, J. A. 1971 A computing method for incompressible flows bounded by moving walls. *J. Comp. Phys.* **8**, 119.

WHITE, C. M. 1929 Streamline flow through curved pipes. *Proc. R. Soc. Lond.* A **123**, 645.

WILLIAMS, G. P. 1969 Numerical integration of the three-dimensional Navier–Stokes equations for incompressible flow. *J. Fluid Mech.* **37**, 727.

WILLIAMS, G. S., HUBBELL, C. W. & FENKELL, G. H. 1902 Experiments at Detroit, Mich., on the effect of curvature upon the flow of water in pipes. *Trans. ASCE* **47**, 1.

YAO, L.-S. & BERGER, S. A. 1975 Entry flow in a curved pipe. *J. Fluid Mech.* **88**, 339.